Offshore Metallic Platforms Observation Using Dual-Polarimetric TS-X/TD-X Satellite Imagery: A Case Study in the Gulf of Mexico

Armando Marino, *Member, IEEE*, Domenico Velotto, *Member, IEEE*, and Ferdinando Nunziata, *Senior Member, IEEE*

***Abstract*—Satellite-based synthetic aperture radar (SAR) has been proven to be an effective tool for ship monitoring. Offshore platforms monitoring is a key topic for both safety and security of the maritime domain. However, the scientific literature oriented to the observation of offshore platforms using SAR imagery is very limited. This study is mostly focused on the analysis and understanding of the multipolarization behavior of platforms' backscattering using dual-polarization X-band SAR imagery. This study is motivated by the fact that under low incidence angle and moderate wind conditions, copolarized channels may fail in detecting offshore platforms even when fine-resolution imagery is considered. This behavior has been observed on both medium- and high-resolution TerraSAR-X/TanDEM-X SAR imagery, despite the fact that platforms consist of large metallic structures. Hence, a simple multipolarization model is proposed to analyze the platform backscattering. Model predictions are verified on TerraSAR-X/TanDEM-X SAR imagery, showing that for acquisitions under low incidence angle, the platforms result in a reduced copolarized backscattered intensity even when fine resolution imagery is considered. Finally, several solutions to tackle this issue are proposed with concluding remark that the performance of offshore observation.**

***Index Terms*—Maritime safety and security, offshore platforms, polarimetry, radar, synthetic aperture radar (SAR), target detection.**

I. Introduction

TODAY oil and gas extraction is mostly onshore; however, the recent discovery of a significant number of deposits in the seabed increased the amount of offshore installations [1]. A complex infrastructure is required to drill wells, extract, process, and temporarily store crude oil and natural gas; hence, for operational reasons, the offshore installations were restricted to shallow waters, such as the North Sea, till the advent of deep water drilling technologies. The increased number of installations, the nature of mechanical drilling operations, and extreme weather situations (e.g., hurricanes) make offshore platforms potential environmental threats. One example is the well oil blowout at the Deepwater Horizon platform drilling site in the Gulf of Mexico (GoM). Furthermore, since floating production system is dynamically positioned, they are obstacles for yachts, merchant ships, and low flying airplanes creating potential threats to the safety of maritime traffic [2]. In conclusion, a continuous monitoring of offshore platforms is a matter of maritime safety and environmental security.

Traditional surveillance techniques, like coastal-based radars, flight surveys, or patrol control can provide abundant information on platforms locations, but only with limited spatial and temporal coverage and at a high cost for equipment and manpower. Platforms owners have obviously all the information needed to create an updated database, but they are usually adverse in sharing this data with competitors or publically for business reasons. However, thanks to the huge development in Earth observation satellites, such information can be accessed at relatively low cost, over large areas, and in a regular manner.

The monitoring of ocean metallic targets, i.e., ships and oil/gas rigs/platforms, with satellite-based synthetic aperture radar (SAR) has been proven to be effective because of radar almost all-weather and all-day acquisition capabilities [3]. In principle, any metallic target over the ocean surface is responsible for a lager backscattering, compared to the one coming from the surrounding sea surface. For this reason, offshore platforms are expected to appear in SAR intensity images as spots brighter than the background sea (see Fig. 2(a)). Several algorithms have been developed that detect metallic targets in SAR imagery by searching for bright pixels on a darker background [4]–[10]. Among approaches based on single-polarization SAR architectures, the constant false alarm rate is the most utilized. To improve detection performance, techniques that exploit also the phase contained in single look complex (SLC) SAR data have been proposed [11]–[15]. However, the information provided by backscattered intensity collected by a single-polarization SAR is not always sufficient to effectively observe metallic targets. The availability of SAR satellites with multipolarization capabilities, hereafter PolSAR systems, triggered the development of a number of novel algorithms to detect targets at sea [16]–[25].

Manuscript received July 25, 2016; revised February 9, 2017; accepted June 14, 2017. Date of publication July 10, 2017; date of current version October 5, 2017. This work was supported in part by the ESA-NRSCC Dragon-4 Project ID 32235 entitled "Microwave Satellite Measurements for Coastal Area and Extreme Weather Monitoring." *(Corresponding author: Armando Marino.)*

A. Marino is with the School of Engineering and Innovation, Open University, Milton Keynes MK7 6AA, U.K. (e-mail: armando.marino@open.ac.uk).

D. Velotto is with the Maritime Safety and Security Lab, German Aerospace Center, Bremen 28199, Germany (e-mail: domenico.velotto@dlr.de).

F. Nunziata is with the Dipartimento di Ingegneria, Università di Napoli Parthenope, Napoli 80143, Italy (e-mail: ferdinando.nunziata@uniparthenope.it).

Color versions of one or more of the figures in this paper are available online at http://ieeexplore.ieee.org.

Digital Object Identifier 10.1109/JSTARS.2017.2718584

1939-1404 © 2017 IEEE. Personal use is permitted, but republication/redistribution requires IEEE permission.
See http://www.ieee.org/publications_standards/publications/rights/index.html for more information.

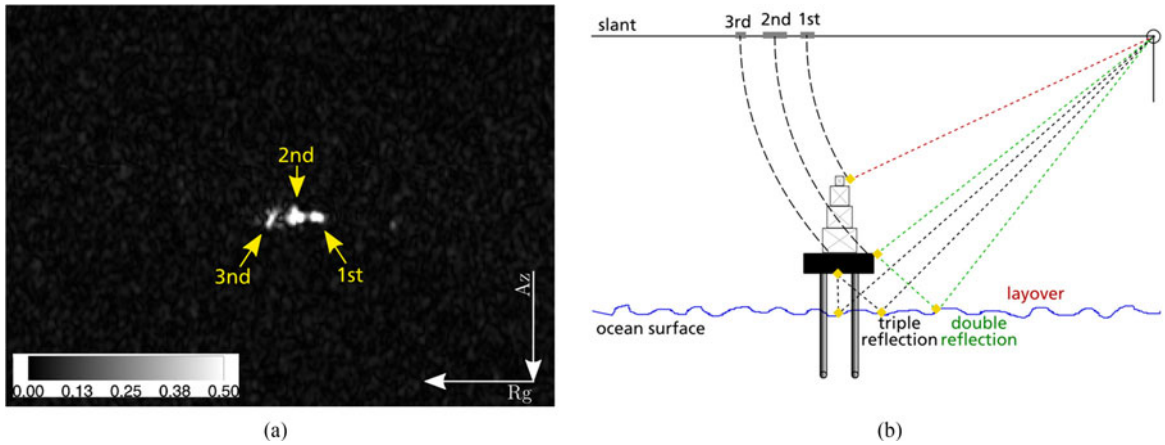

Fig. 1. Schematic sketch of the radar signatures observed in medium-resolution X-band SAR data. (a) TS-X WSC patch showing the typical platform backscatter signature. (b) Schematic sketch of the different signature contributions.

For the purpose of this study, it is worth mentioning that scientific literature focused on the observation of offshore platforms using SAR imagery is very limited. An example of this kind of analysis is given in [26] where Casadio *et al.* have built the database of platforms positions obtained by multitemporal ENVISAT ASAR acquisitions in 2008 for the North Sea area. This *a priori* information has then been used to quantify night-time gas flaring at offshore extractions sites by using along track scanning radiometer. This study clearly witnesses that to ensure temporal sampling dense enough, wide swath SAR imagery is needed. In [27], full-polarimetric SAR measurements are exploited to both observe metallic targets (exploiting combinations of co- and crosspolarized channels) and detect sea oil slicks (exploiting copolarized channels). However, full-polarimetric SAR has a limited swath coverage that may prevent its operational use for offshore platform monitoring.

A. Motivations

In this study, offshore platform monitoring is discussed using dual-polarization X-band SAR imagery. The analysis is undertaken using a dataset of TerraSAR-X/TanDEM-X (TS-X/TD-X) imagery collected over a test site in GoM at low and high incidence angles. The motivation behind this study is the observation that under low incidence angle (around 20°) and moderate wind conditions, copolarized channels may fail in detecting offshore platforms even when fine-resolution imagery is considered. This behavior has been observed at first in medium-resolution TS-X/TD-X single-polarization SAR imagery, despite the fact that platforms are large structures that extend for several tens of meters above the sea level. In order to explain such phenomenon a simple backscattering model is proposed for the platforms. Such model is then tested using dual-polarimetric TS-X/TD-X data. Finally, a detection exercise is performed to show that when copolarized channels are coherently combined, platforms can be successfully observed even at low incidence angles. This witnesses the key role played by the interchannel phase in improving observation performance. This study is mostly focused on the observation and understanding of the polarimetric behavior of platforms and a following work will be carried out in the future that will deal with the comparison of different detectors to understand which one should be used in each acquisition conditions.

The remainder of this paper is structured as follows: In Section II, the backscattering model is briefly sketched; in Section III, multipolarization platforms backscattering are analyzed using actual SAR imagery; while in Section IV, detection performance is discussed using both coherent and incoherent dual-polarimetric features. Finally, conclusions are drawn in Section V.

II. Backscattering Model

To introduce the platform backscattering model, a region of interest extracted from medium-resolution X-band SAR data, that includes sea surface and the target under investigation, is shown in slant range—azimuth coordinate in Fig. 1(a). Note that the spatial resolution is 2.6 m $\times$ 40 m (slant-range x azimuth) and the incidence angle at the platform location is $\theta = 39°.6$. Platforms installed in shallow water consist of vertical metallic towers sustained by submersed pylons fixed to the sea floor. Fig. 1(b) shows an interpretation of the different scattering contributions for a given azimuth angle. The tower's altitude can be of several tens of meters, and, hence, it may cause several scattering mechanisms that results in multiple bright spots aligned along the range direction (indicated by the yellow arrows in Fig. 1(a)). The first mechanism is due to what is commonly referred as layover (dashed red line path in Fig. 1(b)): the direct reflection from the highest structures of the platform and it will be located before the actual position of the platform. The second mechanism is mainly caused by double reflections between the platform vertical structures and the ocean surface (dashed green line path in Fig. 1(b) with yellow diamonds indicating the possible point of reflections): this spot will be located vertically underneath the vertical structure. The third mechanism accounts for triple reflections (or even higher order) between the platform and the surrounding sea surface (dashed black line path in Fig. 1(b)). They could be due to the electromagnetic

wave that reflects on the sea, a platform structure, again on the sea, and back to the sensor (see yellow diamonds along with the dashed black path in Fig. 1(b)). They are located after the platform, since the path that the electromagnetic wave has to travel is longer. According to this simplistic model, these three main mechanisms make possible the detection, and, hence, the platform monitoring using SAR data.

A. Observing the Backscattering of Offshore Platforms With Medium-Resolution Data

Offshore drilling sites consist of several platforms that, when jointly connected, form superstructures whose size is several tens of meters. However, in many cases, offshore platforms are spread a part over the oil field; this happen for instance in GoM [2]. In the case of a wide spatial distribution of platforms, the use of scanning SAR (ScanSAR) imaging mode is a reasonable choice. With this SAR imaging mode, larger coverage is obtained at the cost of lower spatial resolution.

The TS-X/TD-X four beams ScanSAR mode achieves a swath width of ∼100 km at spatial resolution of ∼18 m. In 2013, the TS-X/TD-X product portfolio has been extended adding a six beams Wide-ScanSAR (WSC) mode with ∼40-m resolution and swath width of ∼250 km. Fig. 2(a) shows the UTM map of a projected and calibrated HH-polarized TS-X WSC amplitude image. The image was collected on August 14, 2014 at 12:08 UTC under low-moderate wind conditions (2–5 m/s) over a cluster of offshore platforms in GoM. It is interesting to note that not all bright pixels in Fig. 2(a) are offshore platforms, as other marine metallic targets, e.g. ships, buoys, etc., produce a backscattered signal larger than the sea background one. To classify the bright pixels in Fig. 2(a), the offshore platform records from the U.S. Bureau of Safety and Environmental Enforcement (BSEE) are merged with a cloud-free multispectral image collected by the operational land imager (OLI) onboard the Landsat-8 satellite. The colocated portion of the OLI image is shown in true color composite (band 4 in red, band 3 in green, band 2 in blue) in Fig. 2(b). The figure is augmented with red squares, which indicate the matches between the BSEE dataset and platforms localized in the OLI subimage. A zoom in of one of the platforms (200 × 200 pixels) is shown in the clip on the bottom right side of the image.

B. Results of the Analysis

Comparing Fig. 2(a) and (b), it is possible to conclude that most of the bright pixels in the scene of Fig. 2(a) are offshore platforms. Unfortunately, the physical dimensions of these targets are unknown, but the zoom-in clip of the OLI image (which has a pixel spacing of 30 m) suggests these targets have dimensions larger than 30 m. Besides, oil rigs can be several tens of meters higher than the sea level, and, therefore, they should be detectable in medium-resolution SAR images as well (see Fig. 2(a)). However, one can note that the radar backscatter of such big targets reduces significantly (apparently it vanishes) under certain incidence angles. To better clarify this point, an additional TS-X WSC scene, collected on May 1, 2014 at 12:17 UTC over the same cluster of platforms in Fig. 2(a) and (b), is

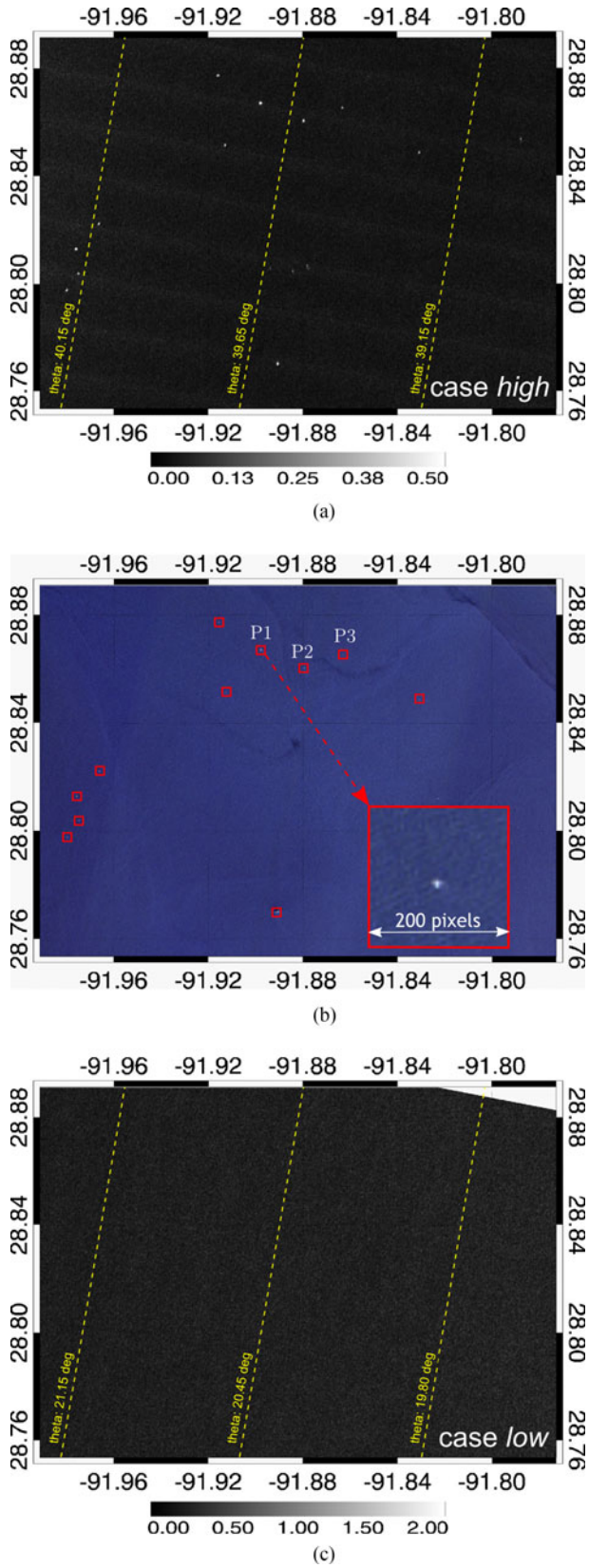

Fig. 2. Cluster of offshore platforms in GoM. (a) Map projection of the calibrated HH-polarized amplitude TS-X WSC mode SAR data collected on 14 August, 2014 (case *high*); (b) true color composite OLI image augmented with BSEE platforms records matches; and (c) map projection of the calibrated HH-polarized amplitude TS-X WSC mode SAR data collected on 1 May, 2014 (case *low*).

TABLE I
OVERVIEW OF THE DUAL-POLARIMETRIC TS-X/TD-X SM ACQUISITIONS OVER KNOWN OFFSHORE PLATFORMS IN GoM

Acquisition *ID*	Data *Time*	Resolution* *Rg-Az*	Incidence Angle ϑ	Polarization	Wind Speed m/s
GoM1	2014/10/13 12:17 UTC	1.2 m × 6.6 m	19.8°–21.7°	HH-VV	7–12
GoM2	2014/03/24 12:08 UTC	1.2 m × 6.6 m	39.0°–40.3°	HH-VV	6–11
GoM3	2012/10/28 12:17 UTC	1.2 m × 6.6 m	19.8°–21.7°	HH-HV	8–12
GoM4	2014/03/02 12:08 UTC	1.2 m × 6.6 m	39.0°–40.3°	HH-HV	5–10
GoM5	2012/11/08 12:17 UTC	1.2 m × 6.6 m	19.8°–21.7°	VH-VV	5–10
GoM6	2014/03/13 12:08 UTC	1.2 m × 6.6 m	39.0°–40.3°	VH-VV	4–9

*Nominal values. The resolution in range depends on incidence angle and increases with it.

considered. The UTM projected HH-polarized amplitude image is shown in Fig. 2(c). Both SAR data are characterized by the same polarization, imaging mode, resolution, and viewing direction. The only difference is the incidence angle, which ranges in the interval 39°.15–40°.15 (case *high*) and 19°.80–21°.15 (case *low*) for the scene shown in Fig. 2(a) and (c), respectively. It can be noted that none of the platforms observed in Fig. 2(a) (and identified in Fig. 2(b)) results in a backscattered signal larger enough to be clearly identified in Fig. 2(c). This outcome might provide an operational constraint when observing offshore platform with single-polarization SAR. Therefore, deeper analysis of the radar backscatter under different polarization combinations and incidence angles is performed in the next section.

III. OBSERVING THE BACKSCATTERING OF OFFSHORE PLATFORMS WITH HIGH-RESOLUTION DATA

In this section, a multipolarization analysis of the signal backscattered by offshore platforms is undertaken exploiting a time series of fine-resolution satellite TS-X/TD-X images collected over the same area under different incidence angles.

A. Dual-Polarimetric Dataset Description

The TS-X/TD-X dataset has been collected in all possible dual-polarization combinations at two different viewing geometries using repeat pass acquisitions. All products have been acquired during satellite descending orbit (right looking) in StripMap (SM) mode which provides a nominal spatial resolution of 1.2 m × 6.6 m (range x azimuth) and the L1b SLC data format is processed. The SAR dataset is described in Table I.

This dataset consists of three couples (one for each dual-polarization combination) of images collected over the same cluster of platforms shown in Fig. 2 at two different incidence angles that, hereinafter, are referred as *low* (GoM1, GoM3, and GoM5) and *high* (GoM2, GoM4, and GoM6).

In Fig. 3, an overview of the area under investigation is shown together with the satellite ground coverages of the *low* (yellow rectangle) and *high* (green rectangle) acquisition geometries. It can be noted that satellite coverages are almost spatially colocated and include several offshore platforms (gray dots). In addition, bathymetry information provided by the NGDC coastal relief model, witnesses that platforms are located in water depth <100 m, hence they are *Fixed type* offshore platforms.

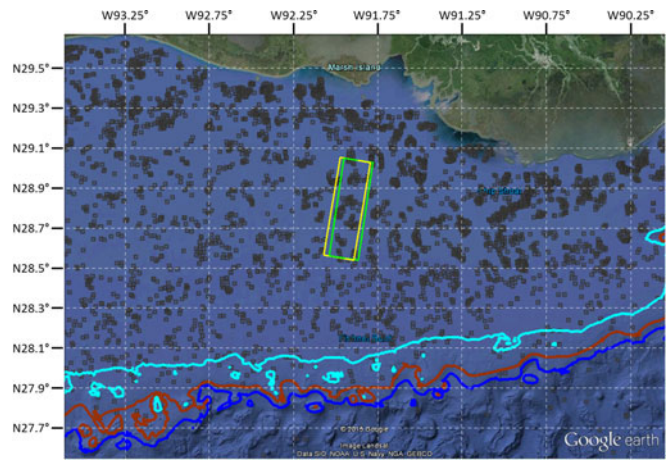

Fig. 3. Overview of the area under investigation (background GoogleEarth). TS-X/TD-X coverages, related to *low* and *high* acquisition geometries, are shown as yellow and green rectangles, respectively. The GoM bathymetry from the NGDC coastal relief model is overlaid as isobath for 100, 200, 300 m depth (cyan, red, and dark blue lines, respectively). Offshore platforms locations are indicated as gray rectangles.

B. Single-Pol Analysis

To analyse the backscattering behaviour of the offshore platforms under different linear transmit/receive polarizations and with respect to the incidence angle, the four dual-polarimetric HH-HV and VH-VV SM TS-X/TD-X are considered, i.e., GoM3 and GoM5 for the case *low* and GoM4 and GoM6 for the case *high*. To make clearer the analysis, we will focus on three platforms randomly selected among all the platforms present. These are termed as P1, P2, and P3 in Fig. 2(b). The geographical location for these platforms is provided in form of maps for an easy cross reference among the results provided in the paper.

In the following, the *low* and *high* incidence angle cases are treated separately.

1) The intensity images for the *low* incidence angle case are shown in Fig. 4. The first row of images refers to the GoM3 acquisition, while the second row refers to the GoM5 one. All the images are ground projected and calibrated magnitudes. The figure is organized in such a way that the images on the main diagonal (see Fig. 4(a) and (d)) refer to copolarized HH and VV channels; while the off-diagonal images (see Fig. 4(b) and (c)) refer to the crosspolarized HV and VH channels. Starting from the copolarized backscattering, it can be observed that it is very hard to

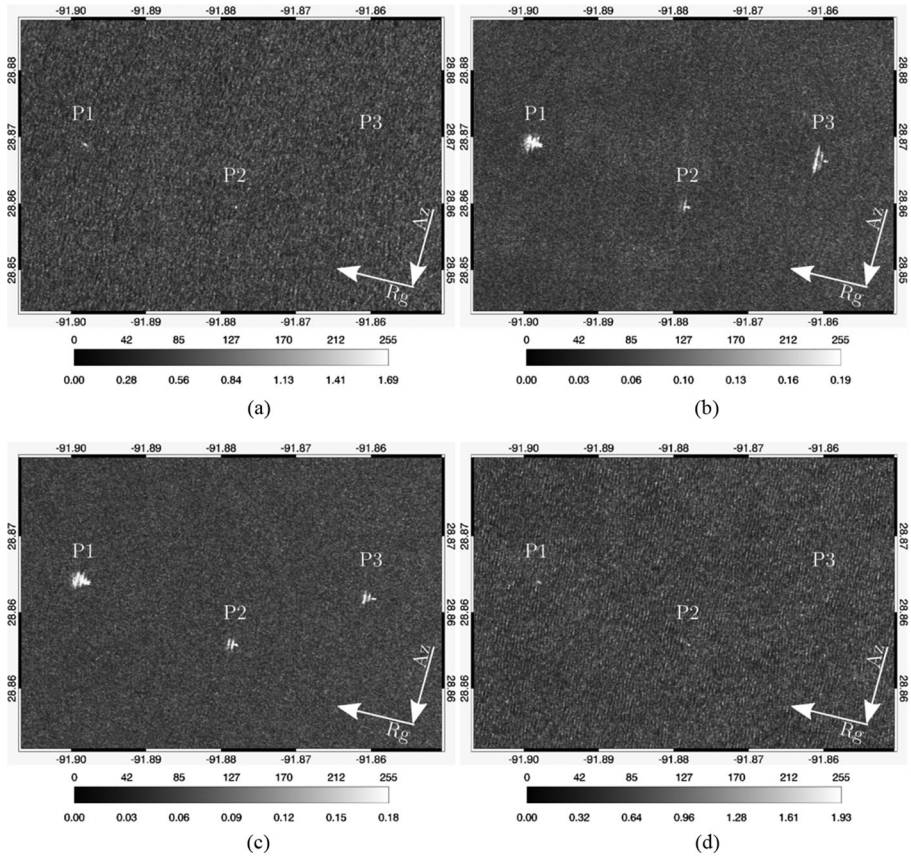

Fig. 4. Multitemporal ground projected calibrated amplitude SAR data collected by TS-X/TD-X over a cluster of three offshore platforms in GoM (labeled as P1, P2, and P3). The first row shows GoM3 imagery collected at HH (a) and HV (b) polarization. The second row shows GoM5 imagery collected at VH (c) and VV (d) polarization.

distinguish the signatures of the three platforms from the surrounding sea surface backscattering. This is especially true for P3. However, if we consider the crosspolarized channels, the platforms are well distinguishable from the surrounding sea clutter. It is interesting to notice that if we compare the results of using high-resolution images (see Fig. 4) with low-resolution images (see Fig. 2), one can conclude that the lower spatial resolution is not playing a key role in making the copolarized backscattering of the platform being undistinguishable from sea clutter.

2) The *high* incidence angle case is analyzed in Fig. 5, where the same format of Fig. 4 is adopted. In this occasion, the first and second rows are referring to the acquisitions GoM4 and GoM6, respectively. It can be noted that all the platforms can be clearly distinguished from the background sea regardless the use of co- or crosspolarized channels. Interestingly, the finer spatial resolution of the SM imagery allows observing the expected signatures resulting from double and triple reflections (see Fig. 1). They appear as elongated strips oriented along the azimuth direction.

C. Scattering Mechanism Analysis

This section aims at analyzing the platforms' backscattering exploiting multipolarization SAR imagery. The images are exploited to gain some understanding on the physics of platform scattering. In particular, a physical explanation of the odd results provided by copolarized imagery collected at low incidence angles is provided. All the information regarding the polarimetric scattering is contained in quad-polarimetric data. Unfortunately, only dual-polarization coherent SAR measurements are available. Among the dual-polarimetric channel combinations, the copol/copol ones, i.e., HH − VV, are the most informative. All the analysis conducted will be restricted to the polarimetric space that is observable using the copolarized combination. The use of quad-polarimetric data may reveal other scattering mechanisms that we are not able to observe using only dual-polarimetric data.

The coherent HH − VV datasets GoM1 and GoM2 (see Table I) are considered and the platform P2 is used as reference. In Fig. 6(a) (case *low*) and (b) (case *high*), false color images are generated normalizing the all *RGB* channels to the span of the covariance matrix. The coding used in this case is: $\text{Red} = |\text{HH-VV}|, \text{Green} = |\text{HH} *(\text{VV})^{\dagger}|$, and $\text{Blue} = |\text{HH}+\text{VV}|$ (where † denotes complex conjugate) in order to highlight double reflection, correlation information, and single reflection, respectively. In other words, for each pixel of these images, the sum of the intensity of HH − VV and HH+VV is unitary. The normalization process is used to get rid of the intensity information and highlight the polarimetric information content. For visualization purposes, Fig. 6(c) (case

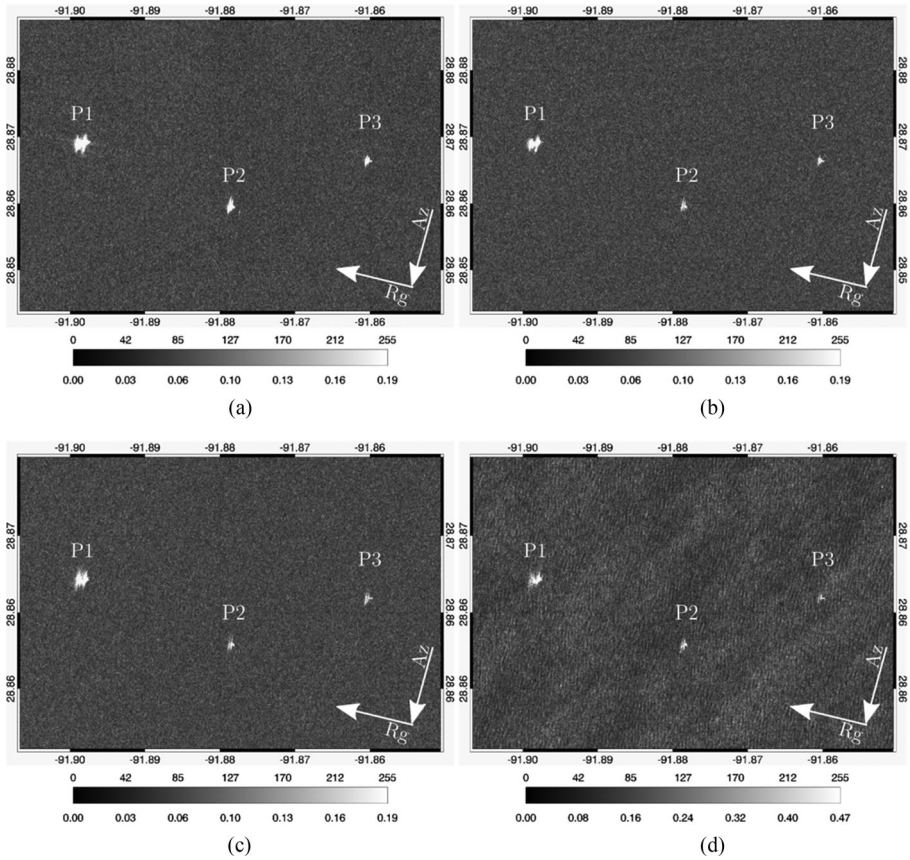

Fig. 5. Multitemporal ground projected calibrated amplitude SAR data collected by TS-X/TD-X over a cluster of three offshore platforms in GoM (labeled as P1, P2, and P3). The first row shows GoM4 imagery collected at HH (a) and HV (b) polarization. The second row shows GoM6 imagery collected at VH (c) and VV (d) polarization.

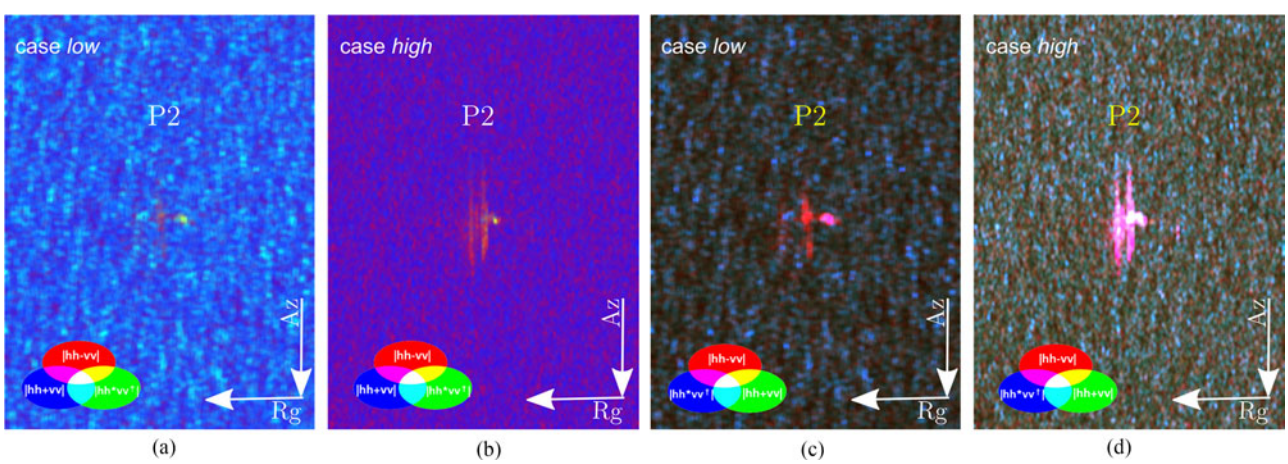

Fig. 6. False color images showing the platform P2 (see Figs. 4 and 5). (a) Dataset GoM1 (case *low*) and (b) dataset GoM2 (case *high*) are normalized using the span and coded as Red = |HH- VV|, Green = $|\mathrm{HH}^*(\mathrm{VV})^\dagger|$, and Blue = |HH + VV|. (c) Dataset GoM1 (case *low*) and (d) dataset GoM2 (case *high*) are scaled using the mean of each channel; Red = |HH - VV|, Green = |HH + VV|, and Blue = $|\mathrm{HH} * (\mathrm{VV})^\dagger|$.

low) and (d) (case *high*) is generated without normalization but simply scaling individually the single RGB channels. The coding used in this case is: Red = |HH- VV|, Green = |HH+VV|, and Blue = $|\mathrm{HH}^*(\mathrm{VV})^\dagger|$. In both the cases, a 5×5 Lee filter is applied to reduce speckle noise. While the interpretation of Fig. 6(c) and (d) is straightforward, the results shown in Fig. 6(a) and (b) deserve to be commented. The *low*- and *high*-incidence angle cases are, therefore, treated separately.

1) With respect to the *low* case (see Fig. 6(a)), it can be noted that sea backscattering is characterized by a high single-bounce mechanism and high HH − VV coherence (bluish color) (Bragg scattering applies as expected). Platform

scattering seems to show the expected three mechanisms. The rightmost part of the platform (the pixels that are closer to the sensor in range direction) is dominated by a mechanism that appears in green that represent correlation between the HH and VV channels. This may be a dipole scattering. The pixels in the middle of the platform are reddish which calls for a mechanism that is dihedral scattering. The dual-reflection mechanism is, therefore, an ordinary horizontal dihedral (double bounce). The leftmost mechanism is hard to visualize and submerged by the return from the sea.

2) With respect to the *high* case (see Fig. 6(b)), sea backscattering still calls for Bragg scattering although the pinkish color indicates a mixture with double-reflection contributions. This may be due to the lower backscattering form the sea Platform backscattering clearly identifies the three mechanisms along the range direction. In fact, in this case (see Fig. 6(b)), the rightmost part of the platform appears to be richer in red (it is more yellowish). It appears a mixture of mechanisms that could lead to a larger dihedral scattering. The pixels in the middle of the platform are reddish calling for dihedral scattering. As a matter of fact, since the reflection coefficient of the metallic platform is larger than the sea one, the platform is expected to be well distinguishable in copolarized imagery.

To understand how much power is scattered by each mechanism we need to consider the images Fig. 6(c) and (d).

In conclusion, dihedral scattering plays an important role in platforms' backscattering. This implies that when the incidence angle reduces, platforms are less visible in copolarized intensity imagery since the total area of the planes representing the dihedral is reduced (because the largest plane has to be the one on the platform vertical structures). From an operational viewpoint, this means that the most critical scenario to detect offshore platforms is achieved when single-polarization copolarized, (HH or VV) imagery is collected at low incidence angles. Improving the spatial resolution from tens of meters (e.g., WSC mode) to meters (e.g., SM mode) does not improve platforms detectability.

Crosspolarization images are less affected by this problem because the HV or VH scattering is less related to the dihedral mechanism. However, crosspolarized acquisitions do not represent the standard SAR mode for geoscience applications. In fact, searching the TS-X/TD-X historical archive, about 70% of the high-resolution dual-polarimetric products are HH − VV with the remaining 30% that includes both copol/crosspol products combinations. The percentage of accessing crosspol imagery greatly decrease (about 1%) when medium-resolution single-pol acquisitions are considered. In addition, since offshore detection is very often corroborative to sea oil pollution monitoring [28], crosspolarized channels are not the best option.

IV. Application of Dual-Polarimetric Observables and Detectors

Moderate wind conditions apply through the processed dataset in Table I. Therefore, the sea state analyzed in this study is restricted to moderate. In the future, we will try to collect a larger dataset where we will hopefully capture different sea states. However, it is interesting to note that even under moderate sea state conditions, may be difficult observing the SAR backscattering signature of offshore platforms. Two polarimetric detectors, namely the Geometrical perturbation polarimetric notch filter (PNF) and the degree of depolarization (DoD) are considered. We also tested other polarimetric observables that can be used to gain understanding of the scattering. These are the product `coPro` and ratio `coRat` of copolarized channels. The latter are incoherent observables, i.e., they do not exploit the interchannel phase.

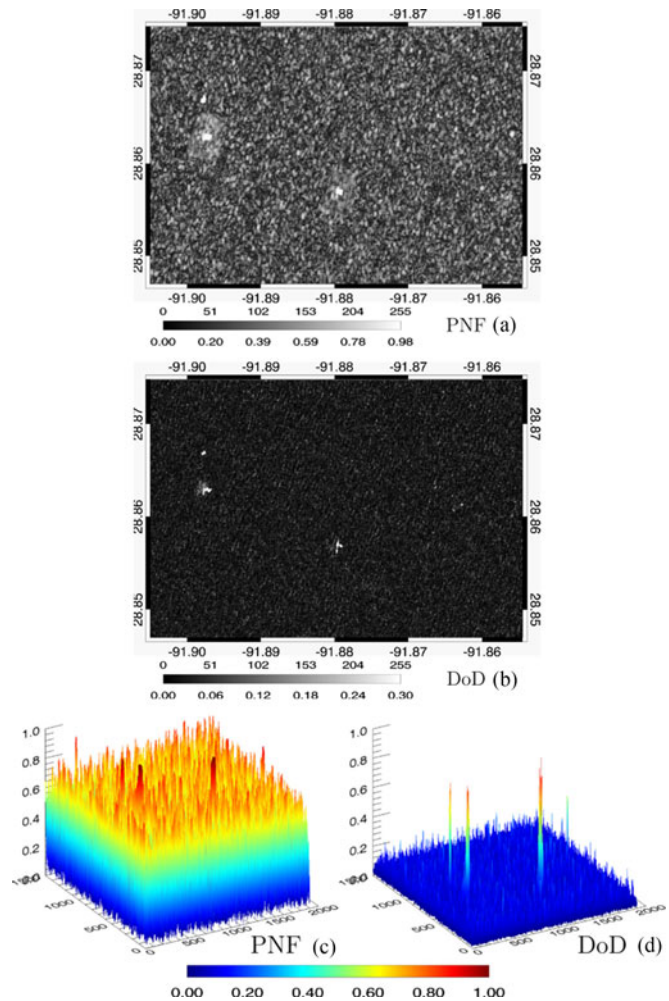

Fig. 7. Case HH − VV *low* incoherent analysis. (a) and (b) ground projected and byte-scaled features coPro and coRat in correspondence of the platforms P1, P2, and P3; (c) and (d) respective normalized 3-D plots in satellite coordinate.

A. Polarimetric Observables and Practical Implementations

The incoherent observables `coPro` and `coRat` are linear combination of the two measured scattering amplitudes and are, therefore, given by

$$\texttt{coProd} = |\mathrm{HH}| * |\mathrm{VV}| \tag{1}$$

$$\texttt{coRat} = |\mathrm{HH}| \,/\, |\mathrm{VV}| \,. \tag{2}$$

In order to take advantage of the polarimetric information, PNF and DoD target detectors have been selected because proposed in the literature as very promising and highly flexible

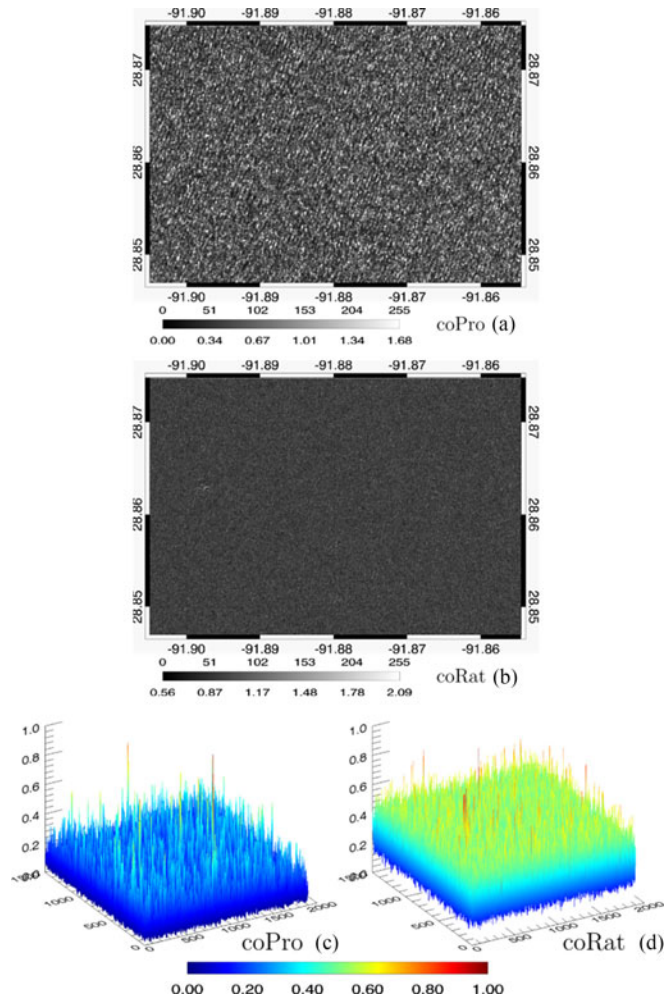

Fig. 8. Case HH − VV *low* coherent analysis. (a) and (b) Ground projected and byte-scaled features PNF and DoD in correspondence of the platforms P1, P2, and P3; (c) and (d) respective normalized 3D plots in satellite coordinate.

for the detection of ships. Their performance for ship detection was shown to exceed the ones obtained via standard single-pol (either copol or crosspol) detectors [18], [21], [25], [29]. It is important to note that their relevance is not limited to copol/copol combination. However, because the purpose of this analysis is to evaluate the effect of the lower backscattering from platforms at low incidence angle, in this study, we dedicate the detection test only to copolarization channels, where the platform is not visible and polarimetry has the potential to improve significantly the detection exercise. The application of detectors to copol/crosspol products and quad-polarimetric data is left for the future, where a larger dataset will be collected to quantify the full benefits of polarimetric information.

The PNF was first proposed by Marino *et al.* [18], [30] and bases the detection strategy on isolating the polarimetric signature coming from the sea and detecting anything else. For this reason, it works as a notch filter in the space of the partial targets, where the null is located on the signature of the sea.

The final detector is obtained by thresholding the polarimetric feature

$$\mathrm{PNF} = \frac{1}{\sqrt{1 + \frac{\mathrm{Red}R}{P_{\mathrm{tot}} - P_{\mathrm{sea}}}}} \tag{3}$$

where $\mathrm{Red}R$ regularize the sensitivity of the distance, and P_{tot} and P_{sea} are the total and clutter powers, i.e., the difference represents the power of the target. In a practical implementation, the signature of the clutter can be extracted locally using large moving windows, while the signature of the target under test can be extracted using smaller moving windows. In this study, the former is extracted locally using 51×51 moving windows, the latter using 5×5 moving windows. For all experiments, $\mathrm{Red}\ R = 0.0025$ has been set. For the detection of ships in dual-polarimetric SAR data, the PNF is suggested to perform best on HH − VV combinations [18], [25], [30].

The DoD is a unitary feature, defined as inverse of the DoP, which represents the distance of the polarization state from the origin of the Poincaré sphere. Since the transmitted waves are always totally polarized, the depolarization is associated with a DoD of the incident states close to unity. As each pixel belonging to a platform can have a different polarimetric scattering mechanisms, the DoD should be higher (more depolarized) on a platform than the surrounding sea surface [21], [29], [31]. The DoD for the dual-polarimetric combination selected is given by equation (4) as shown bottom of this page, where $\Re$ and $\Im$ denote real and imaginary part, respectively. Please note in case of the HH − VV combination, we perform an abuse of notation calling (4) "DoD," since this is applicable only when the same polarized wave is transmitted (in HH − VV, we change the polarization of the transmitted wave). The four terms in 4 are also known as Stokes parameters where the denominator is the total power and used for normalization. In this situation, the physical interpretation of the DoD is not straightforward as for the proper Stokes parameters, but it is still of value in terms of signal processing. As matter of fact in [21], DoD is suggested to perform best on HH − VV among the linear combinations. For the processing of DoD, only a 5×5 moving windows are applied for the estimation.

B. Copol/Copol Case Low

Fig. 7 introduces the incoherent detection exercise for the case HH − VV *low*, where `coPro` and `coRat` features are displayed for the same geographical area shown in Figs. 4 and 5. For a visualization purpose, the incoherent features `coPro` and `coRat` are byte scaled and ground projected in Fig. 7(a) and (b). Additionally, the two features are normalized and displayed in

$$\mathrm{DoD} = 1 - \frac{\sqrt{\left(|\mathrm{HH}|^2 - |\mathrm{VV}|^2\right)^2 + [2\langle\Re(\mathrm{HH} * \mathrm{VV}^\dagger)\rangle]^2 + [2\langle\Im(\mathrm{HH} * \mathrm{VV}^\dagger)\rangle]^2}}{\langle|\mathrm{HH}|^2 + |\mathrm{VV}|^2\rangle} \tag{4}$$

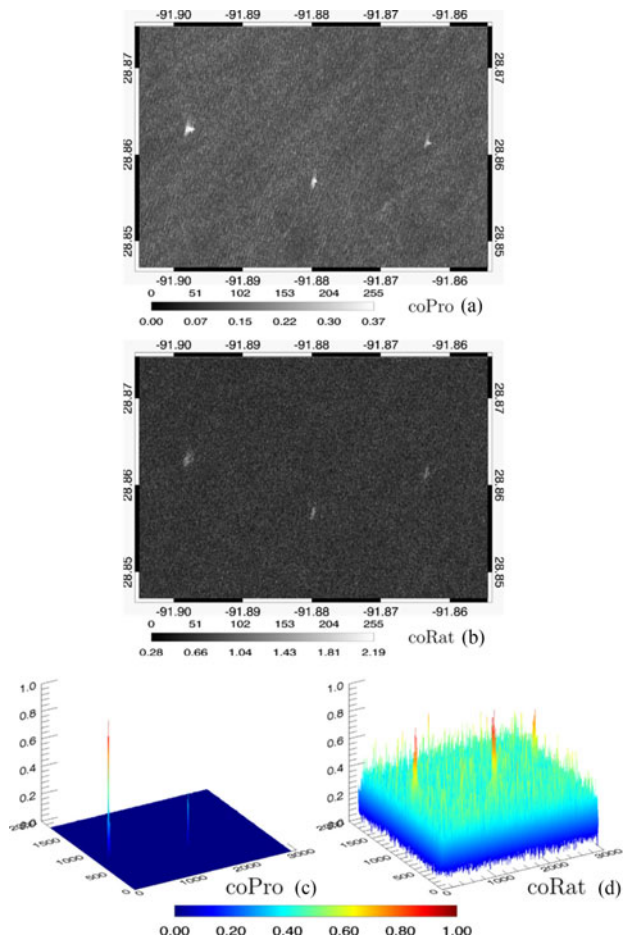

Fig. 9. Case HH − VV *high* incoherent analysis. (a) and (b) Ground projected and byte-scaled features coPro and coRat in correspondence of the platforms P1, P2, and P3; (c) and (d) Respective normalized 3-D plots in satellite coordinate.

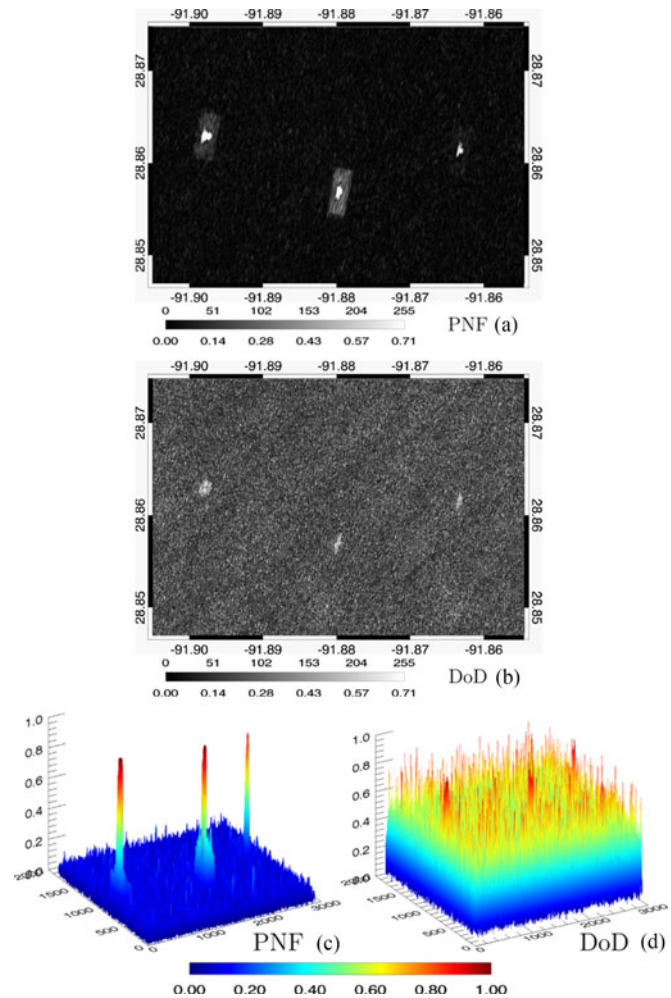

Fig. 10. Case HH − VV *high* coherent analysis. (a), (b) Ground projected and byte-scaled features PNF and DoD in correspondence of the platforms P1, P2, and P3; (c), (d) respective normalized 3-D plots in satellite coordinate.

the form of tridimensional surface in Fig. 7(c) and (d). It can be noted that both incoherent features do not allow observing well-distinguishable signals associated with the platforms present. This implies that the incoherent combination (either product or ratio) do not offer a clear advantage when observing platforms at low incidence angles.

Following the same template, the coherent analysis is introduced in Fig. 8, where PNF and DoD features are considered. In this case, a completely different output is achieved that shows well-distinguishable signals associated with each of the platforms. The additional bright signature located north of the platform on the left-hand side in Fig. 8(a) and (b) is probably a passing by ship, which presence was not possible to recognize before looking at PNF and DoD outputs. Nevertheless, this is a supposition since not ground truth information about ships in the area is available. In summary, these results clearly witness the added value of coherently combining, i.e., both amplitude and interchannel phase copolarized channels for platform detection application.

C. Copol/Copol Case High

For a matter of completeness, we show the obtained results also for the case *high*, although it is not as challenging as the case *low*. Fig. 9 introduces the incoherent analysis for the case HH − VV *high*, where `coPro` and `coRat` features are displayed for the same geographical area shown in Figs. 4 and 5. Similarly, Fig. 10 shows the results of the coherent analysis where PNF and DoD features are considered. In this case, both coherent and incoherent features provide well-distinguishable signals associated with the platforms considered in this investigation.

V. Conclusion

This study aims at analyzing satellite-based SAR observation of offshore sea platforms. A multipolarization analysis is undertaken exploiting a dataset of TerraSAR-X/TanDEM-X multipolarization imagery. It is analyzed and discussed the multipolarization backscattering from platforms at low (around 20°) and high (around 39°) incidence angles. The results obtained clearly shows that platforms, although consisting of relatively large metallic structures, may be hardly visible in single-polarization copolarized SAR imagery collected at low incidence angles under moderate sea state conditions. This phenomenon, which is explained analyzing the scattering contributions that characterize platform backscattering, is significantly mitigated

when coherent dual-polarimetric copolarized acquisitions are exploited. No improvement is obtained when incoherent dual-polarimetric copolarized combinations are exploited. Future research will address the benchmarking of different polarimetric detectors for the cases considered here including the ones that could take benefit of the crosspol channel.

ACKNOWLEDGMENT

The authors would like to thank DLR for providing the TS-X/TD-X data via the AO project (OCE1045). Offshore platform locations in the Gulf of Mexico are provided as public information by the Bureau of Safety and Environmental Enforcement. They would also like to thank the United States Geological Survey Website from where the Landsat-8 data have been downloaded.

REFERENCES

[1] (2016, Apr. 18). *International Energy Agency*. [Online]. Available: http://www.iea.org/

[2] L. A. Muehlenbachs, M. A. Cohen, and T. Gerarden, "Preliminary empirical assessment of offshore production platforms in the Gulf of Mexico," Resources Future, Washington, DC, USA, Tech. Rep. 10–66, Jan. 2011.

[3] J. C. Curlander and R. N. McDonough, *Synthetic Aperture Radar: Systems and Signal Processing*. New York, NY, USA: Wiley, 1991.

[4] D. J. Crisp. (2004, May). *The State-of-the-Art in Ship Detection in Synthetic Aperture Radar Imagery*. [Online]. Available: http://dspace.dsto.defence.gov.au/dspace/handle/1947/3354

[5] S. Brusch, S. Lehner, T. Fritz, M. Soccorsi, A. Soloviev, and B. van Schie, "Ship surveillance with TerraSAR-X," *IEEE Trans. Geosci. Remote Sens.*, vol. 49, no. 3, pp. 1092–1103, Mar. 2011.

[6] A. Gambardella, F. Nunziata, and M. Migliaccio, "A physical full-resolution SAR ship detection filter," *IEEE Geosci. Remote Sens. Lett.*, vol. 5, no. 4, pp. 760–763, Oct. 2008.

[7] M. Tello, C. Lopez-Martinez, and J. J. Mallorqui, "A novel algorithm for ship detection in SAR imagery based on the wavelet transform," *IEEE Geosci. Remote Sens. Lett.*, vol. 2, no. 2, pp. 201–205, Apr. 2005.

[8] P. W. Vachon, J. W. M. Campbell, C. A. Bjerkelund, F. W. Dobson, and M. T. Rey, "Ship detection by the RADARSAT SAR: Validation of detection model predictions," *Can. J. Remote Sens.*, vol. 23, no. 1, pp. 48–59, 1997.

[9] R. L. Paes, J. A. Lorenzzetti, and D. F. M. Gherardi, "Ship detection using TerraSAR-X images in the campos basin (Brazil)," *IEEE Geosci. Remote Sens. Lett.*, vol. 7, no. 3, pp. 545–548, Jul. 2010.

[10] D. Velotto, C. Bentes, B. Tings, and S. Lehner, "First comparison of sentinel-1 and TerraSAR-X data in the framework of maritime targets detection: South italy case," *IEEE J. Ocean. Eng.*, vol. 41, no. 4, pp. 993–1006, Oct. 2016.

[11] J.-C. Souyris, C. Henry, and F. Adragna, "On the use of complex SAR image spectral analysis for target detection: Assessment of polarimetry," *IEEE Trans. Geosci. Remote Sens.*, vol. 41, no. 12, pp. 2725–2734, Dec. 2003.

[12] A. Arnaud, "Ship detection by SAR interferometry," in *Proc. IEEE 1999 Int. Geosci. Remote Sens. Symp.*, 1999, vol. 5, pp. 2616–2618.

[13] K. Ouchi, S. Tamaki, H. Yaguchi, and M. Iehara, "Ship detection based on coherence images derived from cross correlation of multilook SAR images," *IEEE Geosci. Remote Sens. Lett.*, vol. 1, no. 3, pp. 184–187, Jul. 2004.

[14] M. Migliaccio, F. Nunziata, A. Montuori, and R. L. Paes, "Single-look complex COSMO-SkyMed SAR data to observe metallic targets at sea," *IEEE J. Sel. Topics Appl. Earth Obs. Remote Sens.*, vol. 5, no. 3, pp. 893–901, Jun. 2012.

[15] A. Marino, M. J. Sanjuan-Ferrer, I. Hajnsek, and K. Ouchi, "Ship detection with spectral analysis of synthetic aperture radar: A comparison of new and well-known algorithms," *Remote Sens.*, vol. 7, no. 5, pp. 5416–5439, Apr. 2015.

[16] C. Liu and C. H. Gierull, "A new application for PolSAR imagery in the field of moving target indication/ship detection," *IEEE Trans. Geosci. Remote Sens.*, vol. 45, no. 11, pp. 3426–3436, Nov. 2007.

[17] G. Margarit, J. J. Mallorqui, J. Fortuny-Guasch, and C. Lopez-Martinez, "Phenomenological vessel scattering study based on simulated inverse SAR imagery," *IEEE Trans. Geosci. Remote Sens.*, vol. 47, no. 4, pp. 1212–1223, Apr. 2009.

[18] A. Marino, "A notch filter for ship detection with polarimetric SAR data," *IEEE J. Sel. Topics Appl. Earth Obs. Remote Sens.*, vol. 6, no. 3, pp. 1219–1232, Jun. 2013.

[19] F. Nunziata, M. Migliaccio, and C. E. Brown, "Reflection symmetry for polarimetric observation of man-made metallic targets at sea," *IEEE J. Ocean. Eng.*, vol. 37, no. 3, pp. 384–394, Jul. 2012.

[20] M. Sciotti, D. Pastina, and P. Lombardo, "Exploiting the polarimetric information for the detection of ship targets in non-homogeneous SAR images," in *Proc. 2002 IEEE Int. Geosci. Remote Sens. Symp.*, 2002, vol. 3, pp. 1911–1913.

[21] R. Shirvany, M. Chabert, and J.-Y. Tourneret, "Ship and oil-spill detection using the degree of polarization in linear and hybrid/compact dual-pol SAR," *IEEE J. Sel. Topics Appl. Earth Obs. Remote Sens.*, vol. 5, no. 3, pp. 885–892, Jun. 2012.

[22] D. Velotto, M. Soccorsi, and S. Lehner, "Azimuth ambiguities removal for ship detection using full polarimetric X-band SAR data," *IEEE Trans. Geosci. Remote Sens.*, vol. 52, no. 1, pp. 76–88, Jan. 2014.

[23] D. Velotto, F. Nunziata, M. Migliaccio, and S. Lehner, "Dual-polarimetric TerraSar-X SAR data for target at sea observation," *IEEE Geosci. Remote Sens. Lett.*, vol. 10, no. 5, pp. 1114–1118, Sep. 2013.

[24] C. Wang, Y. Wang, and M. Liao, "Removal of azimuth ambiguities and detection of a ship: Using polarimetric airborne C-band SAR images," *Int. J. Remote Sens.*, vol. 33, no. 10, pp. 3197–3210, May 2012.

[25] A. Marino and I. Hajnsek, "Statistical tests for a ship detector based on the polarimetric notch filter," *IEEE Trans. Geosci. Remote Sens.*, vol. 53, no. 8, pp. 4578–4595, Aug. 2015.

[26] S. Casadio, O. Arino, and A. Minchella, "Use of ATSR and SAR measurements for the monitoring and characterisation of night-time gas flaring from off-shore platforms: The north sea test case," *Remote Sens. Environ.*, vol. 123, pp. 175–186, Aug. 2012.

[27] M. Migliaccio, F. Nunziata, A. Montuori, X. Li, and W. G. Pichel, "A multifrequency polarimetric SAR processing chain to observe oil fields in the Gulf of Mexico," *IEEE Trans. Geosci. Remote Sens.*, vol. 49, no. 12, pp. 4729–4737, Dec. 2011.

[28] X. M. Li, T. Jia, and D. Velotto, "Spatial and temporal variations of oil spills in the north sea observed by the satellite constellation of TerraSAR-X and TanDEM-X," *IEEE J. Sel. Topics Appl. Earth Obs. Remote Sens.*, vol. 9, no. 11, pp. 4941–4947, Nov. 2016.

[29] F. Nunziata, A. Gambardella, and M. Migliaccio, "On the degree of polarization for SAR sea oil slick observation," *ISPRS J. Photogramm. Remote Sens.*, vol. 78, pp. 41–49, Apr. 2013.

[30] A. Marino, M. Sugimoto, K. Ouchi, and I. Hajnsek, "Validating a notch filter for detection of targets at sea with ALOS-PALSAR data: Tokyo bay," *IEEE J. Sel. Topics Appl. Earth Obs. Remote Sens.*, vol. 7, no. 12, pp. 4907–4918, Dec. 2014.

[31] J. J. Van Zyl, "Unsupervised classification of scattering behavior using radar polarimetry data," *IEEE Trans. Geosci. Remote Sens.*, vol. 27, no. 1, pp. 36–45, Jan. 1989.

Armando Marino (M'xx) received the M.Sc. degree in telecommunication engineering from the Universita' di Napoli "Federico II," Naples, Italy, in 2006. In 2006, he joined the High Frequency and Radar Systems Department, German Aerospace Centre, Oberpfaffenhofen, Germany, where he developed his M.Sc. thesis. He received the Ph.D. degree in polarimetric SAR interferometry from the School of Geosciences, University of Edinburgh, Edinburgh, U.K., in 2011.

From March 2011 to October 2011, he was with the University of Alicante, Institute of Computing Research, Spain. From December 2011 to May 2015, he was a Postdoctoral Researcher and Lecturer with ETH Zürich, Institute of Environmental Engineering, Switzerland. Since June 2015, he has been a Lecturer with the School of Engineering and Innovation, Open University, Milton Keynes, U.K.

Dr. Marino's Ph.D. thesis received the "Best Ph.D. Thesis 2011" by the Remote Sensing and Photogrammetry Society and the "Outstanding Ph.D. Thesis" by Springer Verlag, which published the thesis in 2012.

Domenico Velotto (S'08–M'15) was born in Italy on April 30, 1981. He received the M.Sc. degree (five-year legal course of study) in nautical science (curriculum electronic radio-navigation and Earth observation systems) from the Università degli Studi di Napoli Parthenope, Naples, Italy, in 2008, and the Dr. Ing. degree in civil, geo, and environmental engineering from the Technical University of Munich, Munich, Germany, in 2016.

He was a Ph.D. Student/Young Research Scientist with the synthetic aperture radar (SAR) oceanography team of the Remote Sensing Technology Institute (IMF), German Aerospace Center (DLR), Wessling, Germany, from March 2009 to February 2013. Since March 2013, he has been a Research Engineer with the Maritime Safety and Security Lab, Signal Processing Department (IMF-SAR), DLR, Bremen, Germany. His main research interests include electromagnetic models, Earth observation with SAR polarimetry, image processing, signal processing, machine learning, and data fusion toward maritime surveillance applications.

Dr. Ing. Velotto received the IEEE GRS South Italy Chapter Best Remote Sensing Thesis Award in 2008.

Ferdinando Nunziata (S'03–M'12–SM'14) was born in Italy in 1982. He received the B.Sc. and M.Sc. degrees (*summa cum laude*) in telecommunications engineering and the Ph.D. degree (curriculum electromagnetic fields) from the Università degli Studi di Napoli "Parthenope," Napoli, Italy, in 2003, 2005, and 2008, respectively.

He was a Guest Professor with Shanghai Ocean University, Shanghai, China. Since 2010, he has been an Assistant professor in electromagnetic fields with the Università degli Studi di Napoli "Parthenope." He is the author/coauthor of about 60 peer-reviewed journal papers. His main research interests include applied electromagnetics, including electromagnetic modeling, single- and multipolarization sea surface scattering, radar polarimetry, synthetic aperture radar sea oil slick and metallic target monitoring, spatial resolution enhancement techniques, and global navigation satellite system-reflectometry.

Dr. Nunziata received the IEEE GRS South Italy Chapter Best Remote Sensing Thesis Award in 2003, the Sebetia-Ter International Award for his research interests in remote sensing in 2009, and the Latmiral Prize provided by the Italian Society of Electromagnetics in 2012. He is a Young Professional (formerly GOLD) representative to the Geoscience and Remote Sensing Society AdCom and to the IEEE Italy Section ExCom.